

Learning Approach to FMCW Radar Target Classification with Feature Extraction from Wave Physics

Kai Tan, Tiantian Yin, Hongning Ruan, Siegfried Balon, and Xudong Chen, *Fellow, IEEE*

Abstract—Target classification is of great value when the number of transceivers in a sensing system is relatively small. This paper proposes a high-accuracy and efficient classification method with machine learning techniques on frequency-modulated-continuous-wave (FMCW) radar. We first establish the novel mapping relationship from physical space to range-Doppler (R-D) image based on wave propagation theory, by which four physical features that effectively capture the kinematic and geometrical characteristics of targets, including speed, total reflectivity, area, and incidence angle, are extracted from R-D image. Then, a multi-layer perceptron with a single hidden layer is employed to realize the classification. Since the above-mentioned four physical features, derived from wave physics, are chosen as the input of the neural network, our classifier does not work in a black-box way. The computational complexity of the whole classifier is the same as that of a 2D FFT, which guarantees a real-time operation. As an example, the proposed classifier is applied to automotive radar system, where road targets are to be classified into five categories, including pedestrian, bike, sedan, truck/bus, and other static objects. Real-world data obtained from 77-GHz FMCW radars are provided for the validation, where the proposed physics-assisted classifier turns out to outperform the state of the art in automotive radar application. The overall accuracy by the real data is about 99% even with complex multiple-target cases.

Index Terms—Automotive radar, frequency modulated continuous wave (FMCW), machine learning, target classification.

I. INTRODUCTION

Due to the advantages such as high range resolution, low transmitting power, small size, low cost, etc., frequency-modulated-continuous-wave (FMCW) radar has been widely used in many traditional applications like meteorological observation [1], navigation [2], [3], free-space

surveillance [4], [5], etc., and also some emerging areas like intelligent traffic monitoring [6], [7], and autonomous driving [8]–[10]. For the applications of radar sensing, imaging is often the most intuitive way. However, radar imaging requires a wide sensing area and a great number of antennas to guarantee the imaging resolution and dynamic level, which can hardly be satisfied for some applications like intelligent transportation and autonomous driving at current stage. In the case of limited observation angle or small number of antennas, target classification is obviously more practical, and in this paper, we mainly study the precise and efficient target classification with FMCW radar.

To distinguish among different kinds of targets, we need first to find as many features of the targets as possible, which vary with the target categories and thus can serve as an effective tool for classification. The common features by FMCW radar sensors can be roughly divided into four types:

- 1) Shape and size. It is easy to understand that different target categories have different shape and size. Such geometrical features can be acquired from 2D imaging results [11]–[15]. To provide the required resolution for realizing the accurate classification, a synthetic aperture with large size is always necessary. This means that a long measurement time of up to a couple of seconds is needed, which obviously cannot meet the requirement of real-time operation for some applications like autonomous driving.
- 2) Micro-Doppler. The increased range and velocity resolutions in current radar sensors have made it possible to measure not only the bulk movement of an object, but also the movement of its individual components, e.g., the rotation of the wheels and even the vibration of the engine. This additional frequency modulation induced by the micro-motions is known as the micro-Doppler effect and has been thoroughly studied in many literatures like [16]–[19]. However, the classification with such a feature requires a certain observation time and thus is unable to implement in real time.
- 3) Radar cross section (RCS). It is obvious that different kinds of objects on the road have different RCS as they always have different shape and size and are made of different materials. Numerical calculations and practical measurements of the RCS distributions of various kinds of objects are studied in [20], [21]. In practical radar applications, the calculation of RCS can be completed within a very short time [22], [23]. Thus, the RCS can serve as an effective tool for real-time classification.

Manuscript received June 2, 2021; revised December 29, 2021 and April 6, 2022; accepted April 9, 2022. This work was supported by the research grant from the Desay SV Singapore Pte. Ltd. (*Corresponding author: Xudong Chen.*)

K. Tan is now with the Key Laboratory for Information Science of Electromagnetic Waves (Ministry of Education), School of Information Science and Technology, Fudan University, Shanghai 200433, China. He was previously with the Department of Electrical and Computer Engineering, National University of Singapore (tankai@fudan.edu.cn).

T. Yin and X. Chen are with the Department of Electrical and Computer Engineering, National University of Singapore, Singapore 117583 (yintiantian@u.nus.edu; elechenx@nus.edu.sg).

H. Ruan and S. Balon are with the Innovation & Technology Center, Desay SV Singapore Pte. Ltd., Singapore 609935 (hongning.ruan@desaysv.com; siegfried.balon@desaysv.com).

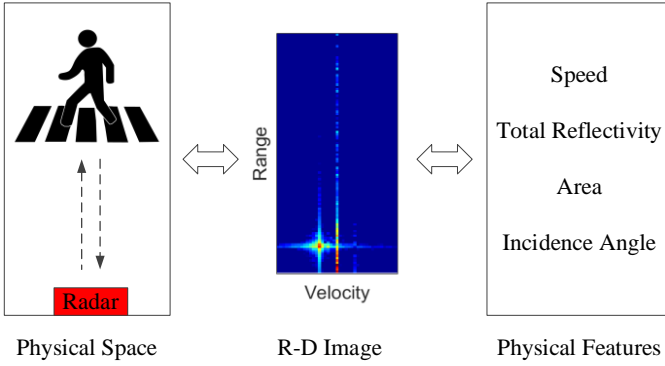


Fig. 1. Illustration of the novel mechanism proposed in this paper. The mapping relationship from physical space to R-D image is established based on wave propagation theory, and the effective physical features of target of interest are then extracted from R-D image following the important mapping relationship.

However, the traditional way of obtaining RCS is based on the calculation of the power of the received A-scan signal, which will inevitably cause inaccuracies when the field of view (FOV) contains multiple targets.

- 4) Others. Some literatures also find several other interesting physical features, such as profiles [24]-[26], natural resonances [27], time-varying track [28], [29], etc. However, these features either have special requirement on measurement condition, or can hardly be available for real-time signal processing.

It is important to note that the signal processing methods of generating the above-mentioned features are completely different. Consequently, it is time-consuming to generate a combination of those features for classification, though more features usually provide more information and thus improve the accuracy of classification. To address this issue, this paper aims to find a fundamental principle that can be used to generate several features of radar target in real time. The fundamental physical principle used here is wave scattering, from which we can easily derive four features of radar targets, including speed, total reflectivity, area, and incidence angle.

In addition to representing physical features of target, the design of classifier is also a key in achieving real-time classification. Currently, machine learning techniques are used to realize the classifications in lots of applications, such as gesture classification [30], [31], human face classification [32], person identification [33], human activity recognition [34], [35], environmental classification [36], automotive radar classification [37]-[40], etc. However, most of these neural networks are used as a purely data-driven black-box classifier. This leads many scholars to spend a lot of efforts in developing various sophisticated neural network architectures that have to use a great deal of unnecessary computational resources to train and learn well-known underlying radar principles.

In order to solve the above-mentioned problems, this paper proposes a novel physical-insights assisted method for multiclass target classification in the application of FMCW radar. The novel mechanism of the proposed method is well illustrated in Fig. 1. The key contributions of the paper can be summarized as the following four points:

- 1) Based on wave theory, the physical space to range Doppler (PS-RD) mapping relationship is established.

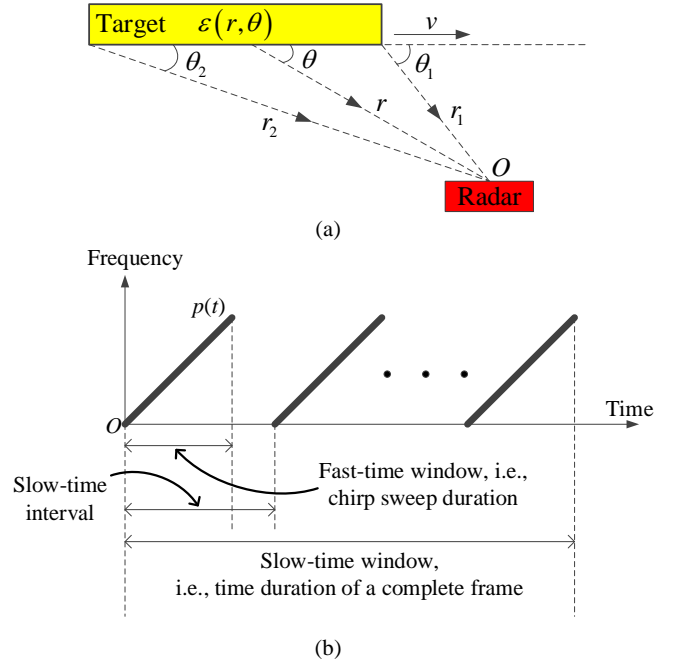


Fig. 2. Illustration of (a) sensing geometry where a single moving target with a certain length is illuminated by radar wave and (b) waveform of the used FMCW signal.

Both the variation of phase and the decay of wave magnitude are considered. Since no special requirement or assumption is made, the mapping relationship can be applied to describe any far-field FMCW radar measurement case.

- 2) Under the important PS-RD mapping, four physical parameters that describe both the kinematic and geometrical characteristics of a moving target, including speed, newly-defined total reflectivity (ToRe), area, and incidence angle, are well formulated. In addition, the high accuracy of R-D image keeps these parameters robust even under multiple-target situation.
- 3) A multi-layer perceptron with a single hidden layer is employed as the classifier, which combines the abovementioned four physical parameters in an appropriate way to realize the target classification. Since the input to the network has as few as four parameters and in addition they are derived from wave physics, our classifier is much more accurate than the neural networks that work in a black-box way when the same amount of training data are used.
- 4) We have provided a detailed analysis of the computational complexity of our algorithm. The computational complexity of the whole classifier is the same as that of generating an R-D map (i.e., 2D FFT), which is computationally cheap and can be realized in real time.

The proposed classifier can be applied to a variety of radar applications where FMCW signal is employed. In this paper, the proposed classifier is applied to automotive radar system, where road targets are to be classified into five categories, including pedestrian, bike, sedan, truck/bus, and other static objects, covering almost all kinds of objects on typical roads. The performance of the proposed method is validated by the

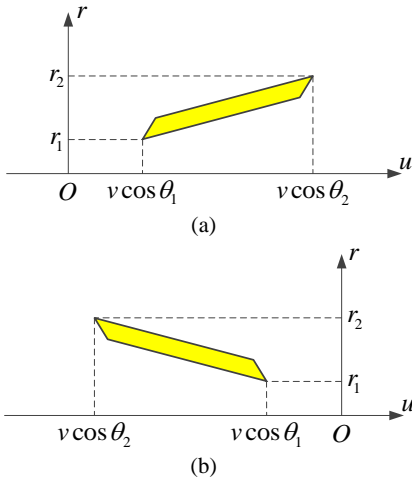


Fig. 3. R-D spectrum corresponding to the sensing model shown in Fig. 2 (a), where a moving target with a certain length and width is illuminated. (a) The case when $v > 0$, i.e., target moves toward radar platform. (b) The case when $v < 0$, i.e., target moves away from radar platform.

real-world data that are measured from various roads with 77-GHz FMCW automotive radars. The measurement data contain both single-target and multiple-target cases, and the testing results show that the proposed classifier outperforms the state of the art in automotive radar application. The overall accuracy by the real data is about 99%.

The rest of this paper is organized as follows. Section II focuses on the formulation of the PS-RD mapping relationship and then Section III gives the way of calculating the four effective physical features. Section IV mainly discusses the used multi-layer perceptron and the computational complexity of the whole classifier. The validation and results are provided in Section V. Finally, conclusions are drawn in Section VI.

II. PHYSICAL SPACE TO RANGE DOPPLER MAPPING

In this section, we will establish the PS-RD mapping relationship by analyzing a general sensing model based on wave theory. Let us consider a sensing model shown in Fig. 2 (a), which displays the geometrical relationship for a general radar sensing measurement. A moving target is illuminated by a radar system, and the speed of the target is v relative to the radar. The range between the target and radar and the incidence angle are denoted by r and θ , respectively. Based on such a geometry, we set up a 2D polar coordinates system and assume that the target has the reflection-coefficient map of $\varepsilon(r, \theta)$.

The transmitting signal has an FMCW waveform, as shown in Fig. 2 (b), which is widely applied in various radar measurements. Each transmitted pulse $p(t)$ is a chirp signal, of which the analytical expression is given as

$$p(t) = A \exp \left[j2\pi \left(f_0 t + \frac{1}{2} K t^2 \right) \right] \quad (1)$$

where A is the wave amplitude, f_0 denotes the carrier frequency, and K represents the chirp constant. Under the first-order Born approximation, the received wave field at the

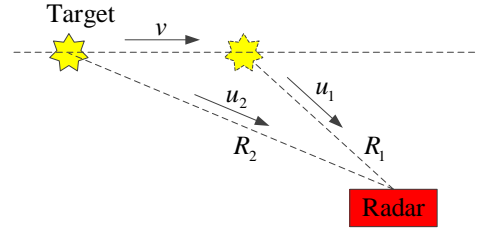


Fig. 4. Illustration of the method of calculating target speed, where the movement between two adjacent frames is utilized.

slow time t_m can be expressed as [41], [42]

$$\begin{aligned} & \tilde{s}_R(t, t_m) \\ &= \iint_S \frac{1}{16\pi^2} \frac{w_T(\theta) w_R(\theta) \varepsilon(r, \theta)}{r^2} p(t - \tau) r dr d\theta \\ &= \iint_S \frac{A}{16\pi^2} \frac{w_T(\theta) w_R(\theta) \varepsilon(r, \theta)}{r^2} \\ & \quad \times \exp \left\{ j2\pi \left[f_0(t - \tau) + \frac{1}{2} K(t - \tau)^2 \right] \right\} r dr d\theta \end{aligned} \quad (2)$$

where the tilde denotes the signal before de-chirping, the integral domain S represents the target region, w_T and w_R are the gain patterns of the transmitting and receiving antennas, respectively, and the time delay is given by

$$\tau = \frac{2(r - ut_m)}{c} = \frac{2(r - vt_m \cos \theta)}{c} \quad (3)$$

where $u = v \cos \theta$ is the velocity along radial direction. After de-chirping, the output signal is obtained as

$$\begin{aligned} & ss_R(t, t_m) \\ &= \tilde{s}_R(t, t_m) \times p^*(t) \\ &= \iint_S \frac{A^2}{16\pi^2} \frac{w_T(\theta) w_R(\theta) \varepsilon(r, \theta)}{r^2} \exp(j\pi K \tau^2) \\ & \quad \times \exp(-j2\pi K \tau t) \exp(-j2\pi f_0 \tau) r dr d\theta \end{aligned} \quad (4)$$

where the superscript $*$ denotes the complex conjugate and $\lambda_0 = c/f_0$ is the wavelength at the carrier frequency. Note that, the tilde is removed for this de-chirped signal. For a general far-field sensing case, the relationship of $r \gg ut_m$ can always be met. Hence, the expression of (4) can be approximated as

$$\begin{aligned} & ss_R(t, t_m) \\ &\approx \iint_S \frac{A^2}{16\pi^2} \frac{w_T(\theta) w_R(\theta) \varepsilon(r, \theta)}{r^2} \\ & \quad \times \exp \left(-j2\pi f_0 \frac{2r}{c} \right) \exp \left[j\pi K \left(\frac{2r}{c} \right)^2 \right] \\ & \quad \times \exp \left[j2\pi \left(-K \frac{2r}{c} \right) t \right] \exp \left(j2\pi \frac{2u}{\lambda_0} t_m \right) r dr d\theta. \end{aligned} \quad (5)$$

Let

$$f = -K \frac{2r}{c} \quad f_m = \frac{2u}{\lambda_0}. \quad (6)$$

Then, (5) can be updated as

$$\begin{aligned}
ss_R(t, t_m) &= \iint_F \exp(j2\pi ft) \exp(j2\pi f_m t_m) \\
&\times \frac{KA^2}{16\pi^2 f_0 v} \frac{w_T(\theta) w_R(\theta)}{f^2 \sqrt{1 - \left(\frac{\lambda_0 f_m}{2v}\right)^2}} r\mathcal{E}(r, \theta) \\
&\times \exp(j2\pi f_0 f / K) \exp(j\pi f^2 / K) df df_m.
\end{aligned} \quad (7)$$

Equation (7) represents clearly a 2D inverse Fourier transform and thus the R-D map is defined as the 2D Fourier transform of (7), i.e.,

$$\begin{aligned}
SS_R(f, f_m) &= \iint_T ss_R(t_m, t) \exp[-j2\pi(f_m t_m + ft)] dt dt_m \\
&= \frac{KA^2}{16\pi^2 f_0 v} \frac{w_T(\theta) w_R(\theta)}{f^2 \sqrt{1 - \left(\frac{\lambda_0 f_m}{2v}\right)^2}} r\mathcal{E}(r, \theta) \\
&\times \exp(j2\pi f_0 f / K) \exp(j\pi f^2 / K).
\end{aligned} \quad (8)$$

Equation (8) establishes the PS-RD mapping relationship, and Fig. 3 roughly illustrates the R-D domain spectrum of the wave model in Fig. 2 (a). The PS-RD mapping is the keystone to extract the physical features of radar target. Compared with the physical features extracted from A-scan wave, the ones calculated based on the R-D spectrum will be much more robust even in multiple-object situations, since different objects can be easily resolved in the 2D R-D image. In addition, according to (6), the angle θ can be obtained from the R-D map as

$$\theta = \arccos\left(\frac{u}{v}\right) = \arccos\left(\frac{\lambda_0 f_m}{2v}\right). \quad (9)$$

Then, the angular accuracy that corresponds to the Doppler resolution df_m in the R-D map can be obtained as

$$\begin{aligned}
d\theta &= \frac{1}{\sqrt{1 - \left(\frac{\lambda_0 f_m}{2v}\right)^2}} \frac{\lambda_0}{2v} df_m \\
&= \frac{\lambda_0}{2v\Delta t_m}, \quad \text{when } f_m = 0
\end{aligned} \quad (10)$$

where Δt_m denotes the width of the slow-time window of a single frame. Take the practical radar system applied in Section V as an example. If the target under test has a velocity of 10 m/s relative to our radar platform, then according to (10), the angular accuracy will be less than 1.4 degree. Such a good azimuthal accuracy from the R-D map is of great help to get the physical features for achieving classification, especially in multiple-target cases.

Furthermore, we need to emphasize that all the above formulation is based on a general sensing model without any special requirements or assumptions. In addition, our entire derivation rigorously obeys wave propagation theory, i.e., both the phase and magnitude information are correctly taken into account. Therefore, the PS-RD mapping relationship given in (8) can be applied to a wide range of radar applications that involve FMCW far-field measurements.

III. FEATURE EXTRACTION

In this section, we will formulate the analytical expressions of the physical parameters that are the keys of the proposed physical-insights-based classification method. Based on the important PS-RD mapping relationship given in (8), four physical parameters that describe both the kinematic and geometrical characteristics of the object, including speed, ToRe, area, and incidence angle, are well formulated as follows.

A. Speed

It is obvious that the speed of object can give a preliminary classification among such kinds of targets like motor vehicle, non-motor vehicle and pedestrian, since these targets often have a significant difference in speed. Based on the geometrical model shown in Fig. 2, supposing that the target is moving uniformly between two adjacent frames, as shown in Fig. 4, then we can obtain the relative velocity v as

$$v = \text{sgn}(R_2 - R_1) \times \sqrt{\frac{R_2^2 u_2^2 - R_1^2 u_1^2}{R_2^2 - R_1^2}} \quad (11)$$

where R_1 and R_2 denote the distances between radar and target at the two adjacent frames, u_1 and u_2 represent the corresponding measured velocities along radial direction, respectively, and the function $\text{sgn}(\cdot)$ represents taking the plus or minus sign. Note that, for a long target, these parameters can be chosen as the values corresponding to the center position. The absolute velocity of target can be easily obtained when the movement of the radar platform is known. For example, if our radar platform has a velocity of V_0 that is parallel to v , then the absolute speed of the target can be easily obtained as

$$v_a = |v + V_0| \quad (12)$$

which holds no matter v and V_0 are the same sign or not.

B. Total Reflectivity

More accurate classification can be further achieved with the ToRe of target, which can be derived from the R-D spectrum. According to (8) and (9), we have

$$\begin{aligned}
r\mathcal{E}(r, \theta) &= \frac{1}{w_T \left[\arccos\left(\frac{\lambda_0 f_m}{2v}\right) \right] w_R \left[\arccos\left(\frac{\lambda_0 f_m}{2v}\right) \right]} \\
&\times \frac{SS_R(f_m, f) \frac{16\pi^2 v f_0 f^2}{KA^2} \sqrt{1 - \left(\frac{\lambda_0 f_m}{2v}\right)^2}}{\exp(j2\pi f_0 f / K) \exp(j\pi f^2 / K)}.
\end{aligned} \quad (13)$$

We define the ToRe of the target as

$$\begin{aligned}
\text{ToRe} &= \iint_S |\mathcal{E}(r, \theta)| r dr d\theta \\
&= \frac{4\pi^2 c^2}{K^2 A^2} \iint_F \frac{|SS_R(f, f_m)| f^2 df df_m}{w_T \left[\arccos\left(\frac{\lambda_0 f_m}{2v}\right) \right] w_R \left[\arccos\left(\frac{\lambda_0 f_m}{2v}\right) \right]}.
\end{aligned} \quad (14)$$

Note that the above-defined ToRe generally represents the ability of back-scattering of a target and at the same time it has a unit of meter square. Nevertheless, we stress that the ToRe defined in (14) is different from the well-known RCS although

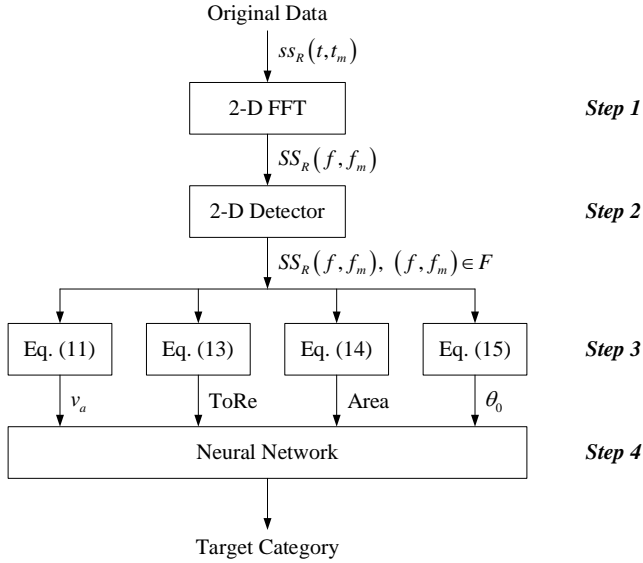


Fig. 5. Flowchart of the proposed classification method.

they share the same units. As long as two targets can be separated in the R-D image, their respective ToRes can be obtained by choosing the corresponding integration domains S in (14). In comparison, RCS involves the power of the total back-scattered field, i.e., the square of the magnitude of the back-scattered field. Since both the square and modulus operators on a complex-valued back-scattered field are nonlinear, it is difficult to obtain individual RCSs when two targets are close to each other.

C. Area

Furthermore, for a target that is moving relative to our radar platform, we can also estimate its geometrical area from the R-D spectrum by

$$\text{Area} = \iint_S r dr d\theta = \frac{c^2 \lambda_0}{8\pi K^2} \iint_S \frac{-f}{\sqrt{1 - \left(\frac{\lambda_0 f_m}{2v}\right)^2}} df df_m. \quad (15)$$

Note that, the area calculated by (15) is in fact the target's reflection area, where the presence of reflection is marked by the regions in the R-D image where the intensity is above a threshold. Note that the integration area S in both (14) and (15) consists of those bins in the R-D image with detectable reflection signals, of which the determination is well described in Section IV. B.

D. Incidence Angle

The observed ToRe and area of the target change with its posture relative to the radar, which is dependent upon the squint angle θ in the wave model of Fig. 2 (a). Therefore, it is necessary to calculate the incidence angle in company with the values of the ToRe and area. The angle of each point in the R-D map has been formulated in (9). For a practical target that occupies a continuous region on R-D map, we use the mean of the angle of target region to represent the incidence angle of target, i.e.,

$$\theta_0 = \left[\arccos\left(\frac{\lambda_0 f_{m1}}{2v}\right) + \arccos\left(\frac{\lambda_0 f_{m2}}{2v}\right) \right] / 2 \quad (16)$$

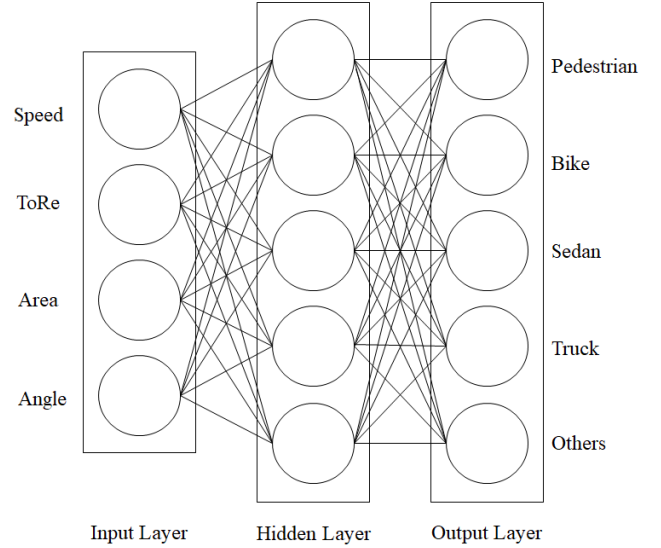


Fig. 6. Architecture of the multi-layer perceptron used in proposed method.

where f_{m1} and f_{m2} denote the minimum and maximum values of f_m within the target region, respectively.

From (11) and (16), it is clear that the calculation of the speed and incidence angle here requires two consecutive frames of data. Nevertheless, one should note that such a calculation guarantees the accuracy of results since the parameters used in (11) and (16) are extracted from the high-accuracy R-D image. In addition, since we only employ R-D maps, our calculation just needs one couple of transmitting and receiving sensors. A possible improvement of this calculation is to obtain the angle θ in a single frame by means of the direction-of-arrival (DoA) techniques, and furthermore, based on the above-mentioned geometrical relationship, the relative velocity can also be calculated easily by

$$v = u / \cos \theta. \quad (17)$$

However, this approach requires a single-input-multiple-output (SIMO) or multiple-input-multiple-output (MIMO) array with a certain length to provide an enough high azimuthal resolution.

IV. MULTI-LAYER PERCEPTRON CLASSIFIER

The proposed classifier can be applied to a variety of radar applications where FMCW signal is employed, since the four physical parameters presented in Section III can describe both the kinematic and geometrical characteristics of a moving target. As an example, the proposed classifier is applied to automotive radar system in this section. We will mainly discuss the architecture and implementation of the applied classifier, as well as its computational complexity.

A. Architecture of the Neural Network

Since the four parameters, analytically given by (12), (14), (15) and (16), are able to well describe the kinematic and geometrical characteristics of a target, there is no need to employ a sophisticated neural network to do the task of classification. In addition, since the numbers of input (four) and output (five) of the network are both small, we employ an existing multi-layer perceptron with a single hidden layer to fulfill the classification. The flowchart of the proposed method

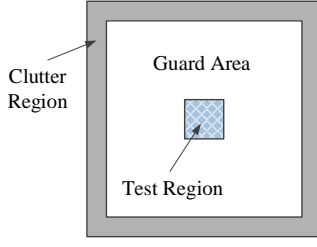


Fig. 7. Illustration of the sliding window employed in 2D CFAR detector that goes through the whole R-D image.

TABLE I. COMPUTATION LOAD OF EACH STEP

Step	FLOPs
1	$5N_s N_m \log_2(N_s N_m)$
2	$15(N_s N_m - 1)$
Eq. (12)	C_1
Eq. (14)	$C_2 N'_s N'_m + 1$
Eq. (15)	$C_3 N'_s N'_m + 1$
Eq. (16)	C_4
4	$2(N_{in} + N_{out})N_{hidden}$
Total	$5N_s N_m [\log_2(N_s N_m) + 3] + (C_2 + C_3)N'_s N'_m + 2(N_{in} + N_{out})N_{hidden} + C$

is shown in Fig. 5, and the architecture of the neural network employed in the proposed method is shown in Fig. 6.

The inputs of the neural network include the four physical parameters, i.e., speed, ToRe, area and incidence angle. The outputs of the neural network are the five categories that are common on the road, including pedestrian, bike, sedan, truck and others like guardrail, bus stop, building, etc. The hidden layer consists of five neurons, of which the activation function is the sigmoid function. The output layer is a softmax layer. The neural network is trained by using the Adam optimizer [43] with a batch size of 8 and a learning rate of 0.001. Note that, the number of hidden layers and neurons are determined after comparing various combinations.

B. Determination of Target Region

According to the formulation in Section II, determination of the target region S is essential in the calculation of the four physical parameters which are used as the inputs of the neural network, especially for multiple-target cases. In order to automatically determine the target region in R-D map, we employ an adaptive and fast constant false alarm rate (CFAR) detector [44], of which the 2D sliding window that goes through the whole R-D image is shown in Fig. 7 and the decision rule is expressed as

$$\Psi = \begin{cases} H_1, & I \geq T_l \\ H_0, & I < T_l \end{cases} \quad (18)$$

where Ψ represents the judgement result, H_1 and H_0 denote the hypothesis that the test region does and does not come from an interested target, respectively, I is the total intensity of the test region, and T_l is the local threshold that depends on the intensity of the clutter region and the pre-set false alarm rate and thus is adaptively obtained for each test region. The sliding

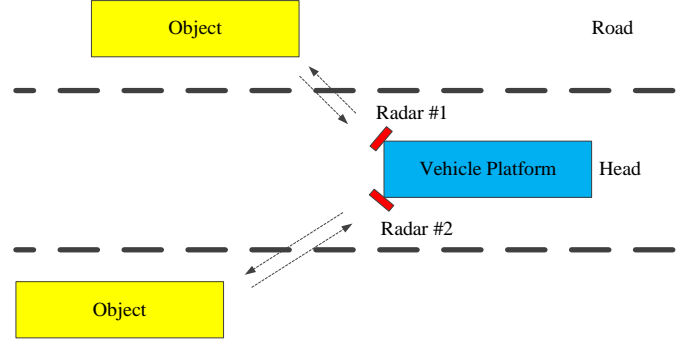


Fig. 8. Configuration of practical measurement on the road with vehicle radars. Thick dotted lines are used to divide different lanes on the road.

TABLE II. SETUP OF APPLIED FMCW RADAR SYSTEM

Carrier frequency	77 GHz
Bandwidth	200 MHz
Chirp sweep duration	12.8 us
Slow-time interval	31.2 us
A/D bandwidth (after de-chirping)	20 MHz
Number of chirps per frame	256
Beamwidth of antenna	140 degree

window will go through the whole R-D image and the regions that are identified as H_1 in (18) collectively constitute the integration area S in (14) and (15).

C. Computational Complexity

In order to evaluate the efficiency of the proposed classifier quantitatively, we further study the computational complexity. Let N_s and N_m denote the number of samples along the range and velocity dimensions of the original R-D map, N'_s and N'_m represent the size of the target region after the detection of (18) (here for the convenience of evaluation, we suppose that the target region has a rectangular shape), and N_{in} , N_{out} and N_{hidden} represent the number of neurons in the input, output and hidden layers, respectively. Under such parameters, the computation load of each step of the flowchart in Fig. 5, which is measured by the floating-point operations (FLOPs), is listed in TABLE I.

In TABLE I, the computation load of the 2D FFT operation in Step 1 is easily obtained. In addition, the computation loads of the fast CFAR detector in Step 2 and the multi-layer perceptron in Step 4 are well studied in [44] and [45], respectively. For the calculation of the four physical parameters in Step 3, the required FLOPs are much lower than those in Steps 1 and 2. The constants C_1 , C_2 , C_3 , C_4 and C in TABLE I account for the computational cost in evaluating such functions as arccosine, square root, modulo, etc. Finally, to make it more intuitive, supposing that all the parameters in TABLE I are in the same order, say N , then according to the total value in TABLE I, the computational complexity of the proposed classifier is obtained as $O(N^2 \log_2 N)$, which is the same as that of a 2D FFT.

V. VALIDATION

In this section, the proposed classification method is validated by a set of real data, which are obtained from practical

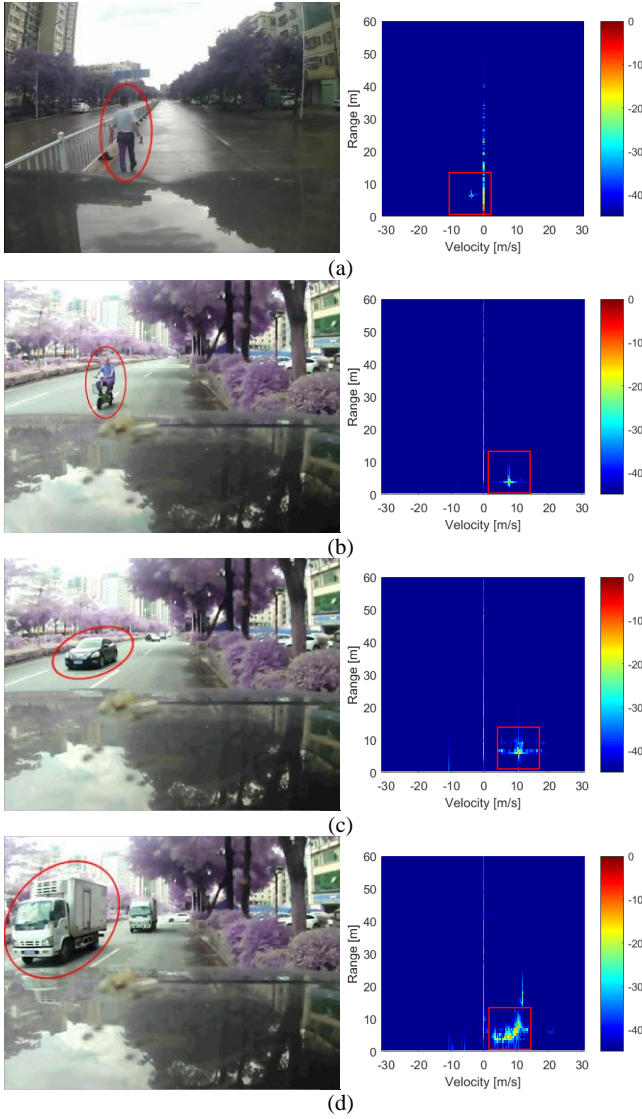


Fig. 9. Four different types of targets that are common on typical roads, including (a) pedestrian, (b) bike, (c) sedan and (d) truck, and their corresponding R-D spectra. In left-side photographs of scenarios, red circle lines are used to identify the target under test. In right-side R-D maps, regions within red square lines, which have the same size of 50×50 bins, contain the target responses. The data are collected when the radar platform is stationary, while the four types of targets are moving.

road driving with 77-GHz FMCW automotive radars. The targets to be classified mainly include five categories that are common on typical roads, i.e., pedestrian, bike, sedan, truck and others. All the algorithms are realized with MATLAB codes. The computation platform is a laptop with a regular 64-bit 2.20-GHz CPU.

A. Measurement

Fig. 8 shows the configuration of our measurement. Two sets of FMCW radars are situated on the left and right corners of the rear of a vehicle platform to acquire object information on both sides. The setups of the employed radar system are summarized in TABLE II. Under the parameters listed in TABLE II, we find that the range of the two dimensions of R-D map are $r \in [0, 192\text{m}]$ and $u \in [-31.22\text{m/s}, 31.22\text{m/s}]$, while the resolutions of them are $dr = 0.75\text{ m}$ and $du = 0.24\text{ m/s}$,

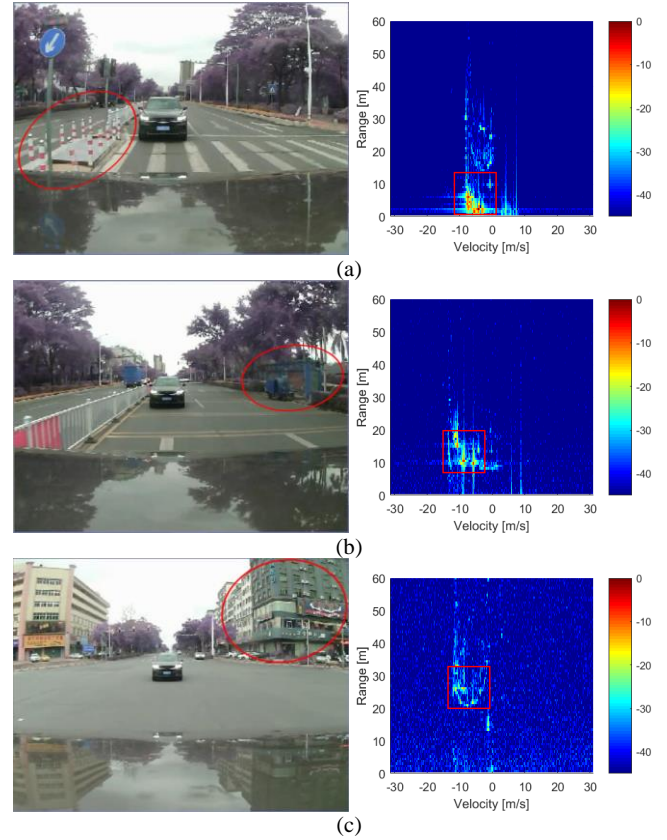


Fig. 10. Other objects on the road that do not belong to the four kinds of common targets shown in Fig. 9, such as (a) guardrail, (b) bus stop and (c) building, and their corresponding R-D spectra. In left-side photographs of scenarios, red circle lines are used to identify the target under test. In right-side R-D maps, regions within red square lines, which have the same size of 50×50 bins, contain the target responses.

respectively.

The photographs and R-D spectra of four kinds of common targets, i.e., pedestrian, bike, sedan and truck, are shown in Fig. 9 and the corresponding results for other types of targets like guardrail, bus station and building are shown in and Fig. 10. Note that, in order to make a fair comparison with other classifiers while ensuring that each input contains only one target, the target regions generated by the CFAR detector are confined within an area of the size of 50×50 bins that corresponds to a range of $12\text{ m} \times 12\text{ m/s}$ (an appropriate zero padding is carried out before taking the 2D FFT to obtain the R-D map), which can effectively cover most of targets in this measurement. The examples of multiple-target cases are shown in Fig. 11. We find in Fig. 11 (c) and (d) that the 2D R-D spectra accurately reflect the cases where multiple targets are moving side-by-side and where guardrail is beside the target of interest. In comparison, as shown in Fig. 11 (e) and (f), the target responses in A-scan wave are very easy to interfere each other under these situations. Such a poor resolving ability of A-scan wave is bound to seriously affect the accuracy of any calculated physical feature based on it.

In this measurement, we provide totally 5000 frames of real data, i.e., 1000 frames for each kind of target, that are extracted from general scenarios on the road, including both single-target and multiple-target situations. For each category, we use 800 frames of data for the training and the validation of the designed

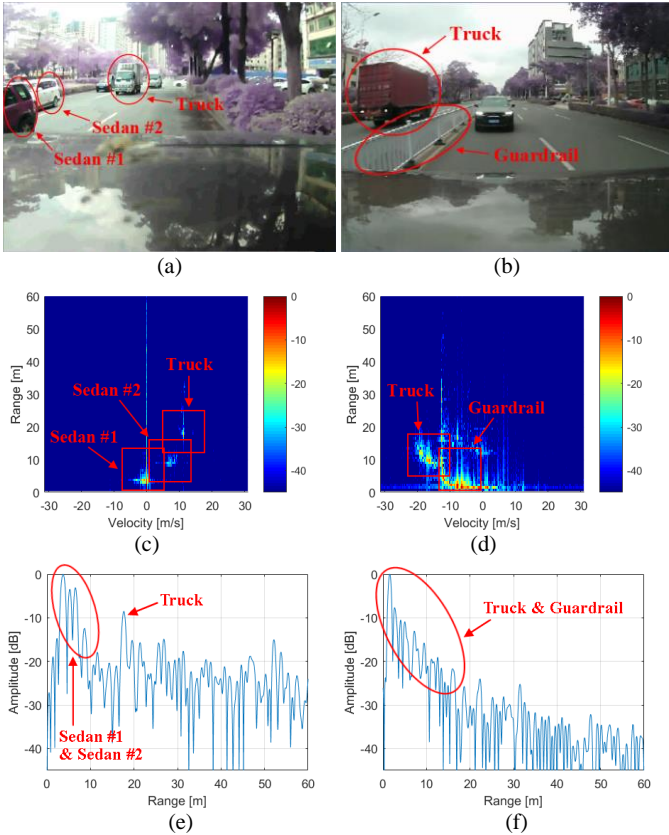


Fig. 11. Examples of cases when FOV contains multiple targets. (a) Photograph of scenario when multiple targets, i.e., sedans and trucks, are moving one after another or side-by-side. (b) Photograph of scenario when a truck is moving nearby guardrail. (c) Corresponding R-D map of (a). (d) Corresponding R-D map of (b). (e) Received A-scan wave of (a). (f) Received A-scan wave of (b). In (a), (b), (e) and (f), red circle lines are used to identify the target under test, while in (c) and (d), regions within red square lines, which have the same size of 50×50 bins, contain the target responses.

neural network, and apply the remaining 200 frames for testing the performance of classifier. The distributions of the four physical parameters, i.e., speed, ToRe, area and incidence angle, that are calculated from both the training/validation data and testing data are clearly displayed in Fig. 12 and Fig. 13, respectively, where we observe that the values of both ToRe and area present marked differences in the five kinds of targets. Furthermore, in order to show more clearly the separation of the proposed ToRe and area among the five target classes, we also plot in Fig. 14 the values of these two features that are calculated from the testing dataset. Note that in the measurement data used here, there is a relative movement between the targets and our vehicle platform, and thus targets can be effectively identified as H_1 in (18). Consequently, the above-mentioned four physical features can be successfully calculated.

B. Methods for Comparison

We compare our proposed classifier with the other three existing methods, which are representative of the state of the art of classification with automotive radar. The first one (i.e., Method #1) and the second one (i.e., Method #2) are both non-machine-learning (non-ML) methods that realize the classification with the input feature and a simple “if-else” logic.

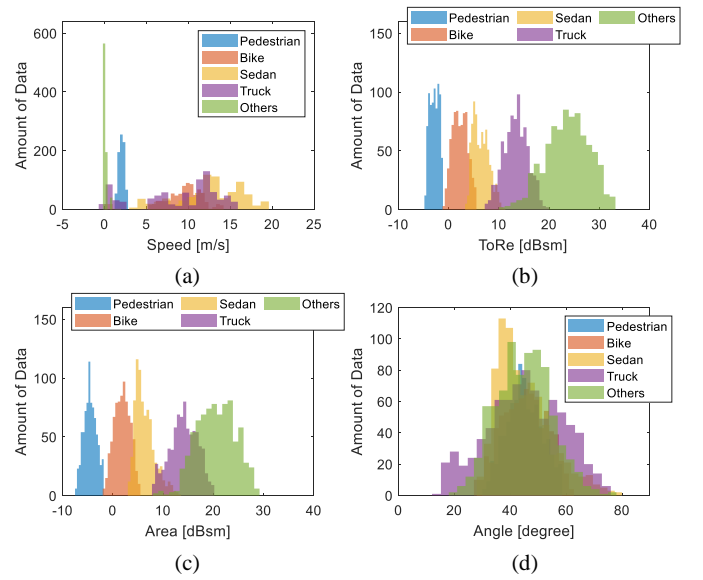


Fig. 12. Distributions of (a) speed, (b) ToRe, (c) area and (d) incidence angle for five kinds of target categories, which are obtained from the training/validation dataset.

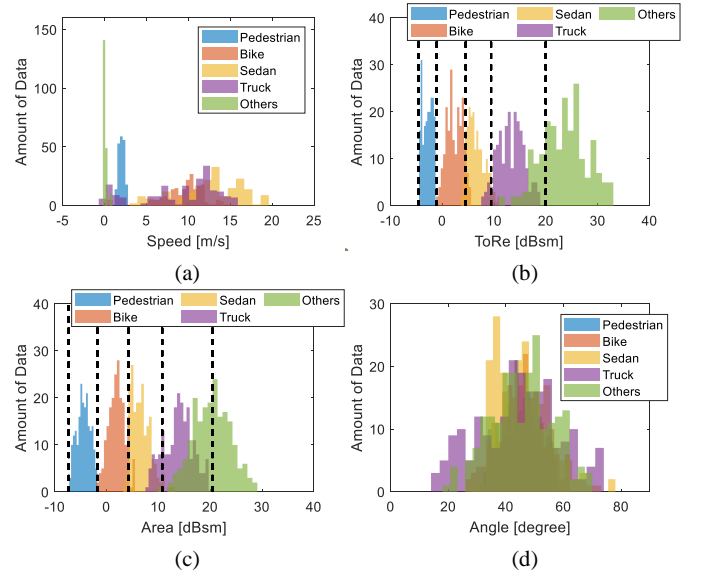


Fig. 13. Distributions of (a) speed, (b) ToRe, (c) area and (d) incidence angle for five kinds of target categories, which are obtained from the testing dataset. Black dotted lines in (b) and (c) represent the thresholds for the classifier used in Method #1.

The block scheme of achieving the classification of five categories with non-ML method is shown in Fig. 15. Method #1 employs the physical parameters studied in this paper as the input feature, while Method #2 uses the root RCS (RRCS) proposed in [23]. The third method (i.e., Method #3) is a CNN-based method studied in [38], where the slices of the region-of-interest (ROI) of the 3D-spectrum are chosen as the input of the neural network. For a fair comparison, the same training and testing datasets are used for the proposed method and the three compared ones. The training dataset are applied for training the neural networks of the proposed method and the Method #3, and are used for obtaining the thresholds employed in Method #1 and #2, i.e., the boundaries of each category that are shown in Fig. 15. The testing dataset are applied for testing

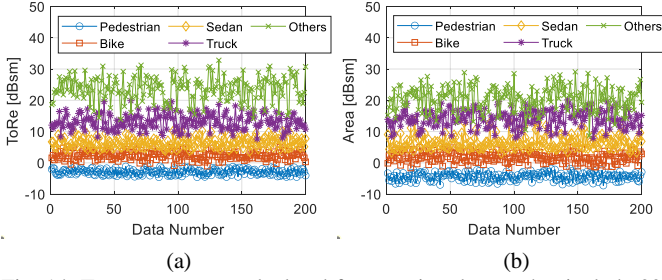


Fig. 14. Two parameters calculated from testing dataset that include 200 frames of range-Doppler maps for each kind of target. (a) ToRe. (b) Area.

the performance of the three methods, as well as the proposed method.

1) Method #1: R-D image-based non-ML method

Since the values of speed and incidence angle significantly overlap among some or even all of the five kinds of targets, these two physical features can hardly be individually applied in the non-ML method that uses “if-else” logic to realize classification. Thus, we employ the calculated ToRe and area values as the input feature, respectively. Fig. 13 (b) and Fig. 13 (c) display the distributions of the ToRe and area obtained from the testing dataset.

2) Method #2: Non-ML method with RRCS

Following the analytical expression provided in [23], the distributions of the RRCS obtained from training and testing dataset are shown in Fig. 16. As we have discussed for Fig. 11 (e) and (f), since the RRCS is obtained from A-scan signal that provides only the range information, the calculated value will not be accurate when the FOV contains multiple targets, and that is why the distributions of RRCS shown in Fig. 16 have more overlaps among different categories than the ToRe and area shown in Fig. 12 and Fig. 13. Such a serious aliasing will certainly affect the accuracy of classification.

3) Method #3: CNN-based method

The CNN architecture is shown in Fig. 17. The input of the CNN is the truncated R-D map with the size of 50×50 bins, which keeps the same size as the area for calculating the proposed physical parameters while guaranteeing each input image only contains a single target. The CNN consists of three convolutional layers with 32, 64 and 128 filters of size 3×3 , respectively. Each convolutional layer is followed by a 2×2 average pooling layer and the last average pooling layer is followed by the fully-connected layers. Batch normalization and drop out with a drop-out probability equal to 0.6 are applied after each fully-connected layer. The Adam optimizer with a batch size of 64 and a learning rate of 0.00001 is applied for the training.

C. Results and Discussion

Since the proposed method and the three compared ones all take very little time (less than 0.1 s) to realize classification, i.e., real-time can be easily achieved by all these methods, we evaluate the performance of algorithm mainly from the accuracy of classification. The confusion matrices of the proposed method and the three compared ones are summarized in TABLES III-VI, while the overall accuracies of all these classification methods are provided in TABLE VII, which are obtained from the corresponding confusion matrices. Furthermore, in order to show the effect of each physical

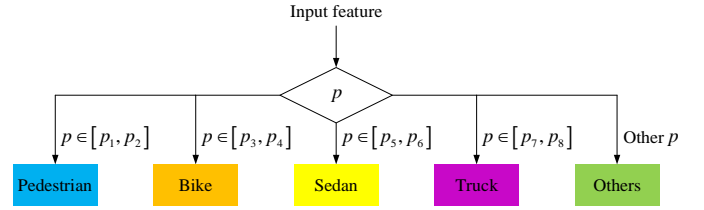


Fig. 15. Block scheme of non-ML method that only uses fixed thresholds and “if-else” logic to realize classification. The extents of different targets have no overlap with each other, which means that the relationship $p_1 < p_2 \leq p_3 < p_4 \leq p_5 < p_6 \leq p_7 < p_8$ is satisfied in this method.

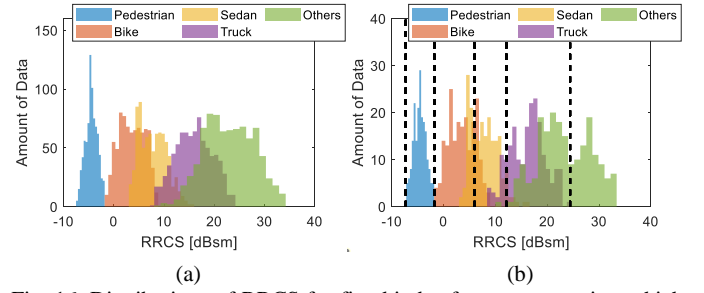


Fig. 16. Distributions of RRCS for five kinds of target categories, which are obtained from the results of (a) training/validation dataset and (b) testing dataset. Black dotted lines in (b) represent the thresholds for the classifier used in Method #2.

parameter in the classification, we summarize in TABLE VIII the accuracies when all four parameters except one are used in the classifier. In addition, we employ 1000 frames of data (200 frames for each kind of target) to test three MLPs with different settings, the testing results are summarized in TABLE IX. From the results in TABLE VII and TABLE VIII, it is clear that the accuracy of classification has a certain reduction when any of the four features is abandoned. The results demonstrate that each input parameter of the classifier represents distinct feature and has its own role in the classification. Then, from TABLE IX, it can be seen that the neural network with 1 hidden layer of 5 neurons has the highest overall accuracy, precision, recall rate and specificity. Meanwhile, there is no significant difference between the computation time using the three kinds of neural networks. Therefore, the neural network with 1 hidden layer of 5 neurons is the best choice.

From the confusion matrices given in TABLES III-VI, we observe that the proposed method provides the highest classification accuracy for each category. Since the proposed neural network deploys the four physical parameters that effectively inherit various characteristics of targets, it has successfully classified all five kinds of targets with an accuracy higher than 99%, which is much higher than those of the other compared methods. In addition, from TABLE VIII we see clearly that the abandonment of any physical parameter will lead to a more or less decrease in the accuracy of classification. In other words, there is no obvious correlation among the four physical parameters, and thus the highest accuracy of classification can be obtained only when all four parameters are employed in the classifier.

For Method #1 and #2, due to the overlap exhibited in the distribution of physical features among different kinds of categories, as shown in Fig. 13 (b), Fig. 13 (c) and Fig. 16 (b), it is easy to understand that the “if-else” logic shown in Fig. 15

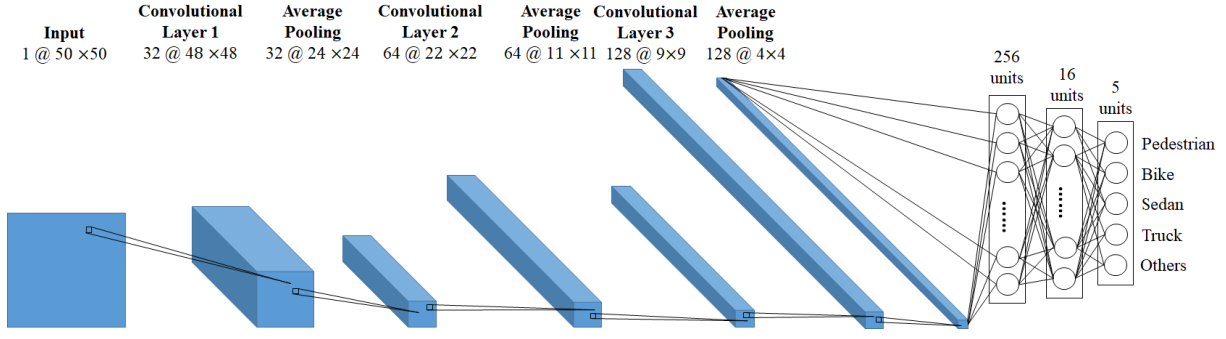


Fig. 17. The architecture of the CNN used in the method for comparison.

TABLE III. CONFUSION MATRIX OF PROPOSED METHOD

	Truth	Prediction				
		Pedestrian	Bike	Sedan	Truck	Others
	Pedestrian	100	0	0	0	0
	Bike	0	100	0	0	0
	Sedan	0	0	100	0	0
	Truck	0	0	0	99	1
	Others	0	0	0	3.5	96.5

TABLE IV. CONFUSION MATRIX OF METHOD #1

A. USING TORe AS INPUT

	Truth	Prediction				
		Pedestrian	Bike	Sedan	Truck	Others
	Pedestrian	100	0	0	0	0
	Bike	0	93.5	6.5	0	0
	Sedan	0	7	88	5	0
	Truck	0	0	10	90	0
	Others	0	0	0	20	80

B. USING AREA AS INPUT

	Truth	Prediction				
		Pedestrian	Bike	Sedan	Truck	Others
	Pedestrian	100	0	0	0	0
	Bike	0	93	7	0	0
	Sedan	0	6	90.5	3.5	0
	Truck	0	0	11	89	0
	Others	0	0	1	40	59

TABLE V. CONFUSION MATRIX OF METHOD #2

	Truth	Prediction				
		Pedestrian	Bike	Sedan	Truck	Others
	Pedestrian	100	0	0	0	0
	Bike	0	79.5	20.5	0	0
	Sedan	0	29	62.5	8.5	0
	Truck	0	0	16	84	0
	Others	0	0	2	58	40

TABLE VI. CONFUSION MATRIX OF METHOD #3

	Truth	Prediction				
		Pedestrian	Bike	Sedan	Truck	Others
	Pedestrian	71.5	2.5	13	8	5
	Bike	13.5	41	38	7.5	0
	Sedan	0.5	8.5	81	10	0
	Truck	0.5	0.5	14	76.5	8.5
	Others	0.5	0	3	1.5	95

TABLE VII. OVERALL ACCURACY

Proposed method	99.1%
Method #1	90.3% (ToRe) and 86.3% (Area)
Method #2	73.2%
Method #3	73.0% ^a

^aThe inferior performance of Method #3 is caused by the small size of training dataset. In other words, the accuracy of Method #3 will be further improved if more training data are available.

TABLE VIII. OVERALL ACCURACY WHEN USING FOUR PARAMETERS EXCEPT ONE

All except Speed	94.1%
All except ToRe	88.2%
All except Area	92.9%
All except Angle	91.8%

TABLE IX. TESTING RESULTS^A BY MLPs WITH VARIOUS SETTINGS

Construction of neural network	Overall Accuracy	Precision	Recall Rate	Specificity	Time
1 hidden layer with 2 neurons	98.7%	98.7%	98.7%	99.7%	26.76 s
1 hidden layer with 5 neurons	99.1%	99.1%	99.1%	99.8%	27.42 s
2 hidden layers with 5 neurons	98.3%	98.3%	98.3%	99.6%	28.10 s

^AThe values of precision, recall rate and specificity are all acquired by macro average [46], and the time is the total prediction time of 1000 samples.

that is adopted in these two methods inevitably leads to certain misjudgment in their classification results. We note that Method #1 obviously outperforms Method #2, which demonstrates the ToRe and area obtained from R-D image are more suitable to deal with various practical situations, especially when the FOV contains multiple objects.

For Method #3, i.e., the CNN-based method, as shown in TABLE VI, bikes are easily classified as sedans and in addition pedestrians are easily classified as sedan by mistake. By contrast, instead of doing feature extraction in a black-box way, the proposed method extracts the features from R-D maps based on the known physical principles, which can well differentiate the five kinds of objects. In addition to the advantage in accuracy, the training time of the proposed method is also much less than that of the Method #3. The reason for this result is that only four physical parameters are chosen as the input of the network in the proposed method, which is much smaller than the dimension of the input of network of Method #3, where the slices of truncated 3D spectrum are directly adopted. With the same computation power, it takes about 2 hours (700 epochs) to train the Method #3, whereas the training of the neural network in the proposed method only requires less than one minute (500 epochs). If we want to improve the classification accuracy of Method #3, the number of training data has to be increased, which however will further increase the training time. From this perspective, we conclude that the proposed method can provide a much higher training efficiency by the application of the physical insights, i.e., high accuracy of classification can be obtained by the proposed method with much fewer training data.

VI. CONCLUSION

In this paper, we propose a method for target classification with FMCW radar. First, based on wave theory, the mapping relationship between physical space and R-D image is established, which uses no any special requirement or assumption and thus can be applied to a wide range of radar applications that involve FMCW far-field measurements. Under such an important relationship, the analytical expressions of four physical parameters that can effectively capture the kinematic and geometrical characteristics of targets, including speed, ToRe, area and incidence angle, are well formulated. In particular, the decay of wave magnitude due to propagation is taken into account in the PS-RD mapping. Since these four parameters are acquired from R-D image that has high accuracy along both range and azimuth dimensions, they can provide an effective discrimination even for multiple-target cases. The proposed classifier can be applied to a variety of radar applications where FMCW signal is employed. As an example, the proposed classifier is applied to automotive radar system, where road targets are to be classified into five categories. The computational complexity of the whole proposed classifier is $O(N^2 \log_2 N)$, which is the same as that of a 2D FFT and guarantees the real-time operation of the classifier. The performance of the proposed classification method is validated by real data obtained from the measurements on practical roads with a self-designed 77-GHz FMCW vehicle radar system. The results show that for the cases that targets can be effectively detected from R-D image, i.e., there is a relative movement between the targets and radar platform, the proposed classification method provides a very high accuracy (about 99%) of classification for the five target categories that is higher than other state-of-the-art techniques like the CNN-based method under the same training dataset. Moreover, compared with the deep learning method that

realizes the classification in a black-box way, the proposed method extracts the effective features from the known physical principles, has as few as four input parameters, and thus provides a much higher training efficiency. In view of these advantages, we believe that such a high-performance classification method is adequately suitable for various FMCW radar sensing applications, especially for the applications like automotive radar, where the performance of the hardware platform is not so powerful due to the restriction of the factors such as size and cost.

ACKNOWLEDGEMENT

The authors would like to very warmly thank the Editors and the anonymous reviewers for their detailed comments and suggestions. The authors would also like to thank the staff of Desay SV for their great help in acquiring and processing the practical measurement data.

REFERENCES

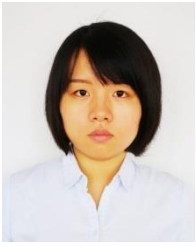
- [1] T. Takano, Y. Nakanishi, and T. Takamura, "High resolution FMCW Doppler radar FALCON-I for W-band meteorological observations," in *Proc. 15th Int. Symp. Antenna Technol. Appl. Electromagn.*, Toulouse, France, 2012, pp. 1-4.
- [2] Y. Wang and Y. Zheng, "An FMCW Radar Transceiver Chip for Object Positioning and Human Limb Motion Detection," *IEEE Sensors J.*, vol. 17, no. 2, pp. 236-237, Jan. 2017.
- [3] E. Jose, M. Adams, J. S. Mullane, and N. M. Patrikalakis, "Predicting Millimeter Wave Radar Spectra for Autonomous Navigation," *IEEE Sensors J.*, vol. 10, no. 5, pp. 960-971, May 2010.
- [4] C. Ding *et al.*, "Continuous Human Motion Recognition With a Dynamic Range-Doppler Trajectory Method Based on FMCW Radar," *IEEE Trans. Geosci. Remote Sens.*, vol. 57, no. 9, pp. 6821-6831, Sept. 2019.
- [5] W. Zhang, H. Li, G. Sun, and Z. He, "Enhanced Detection of Doppler-Spread Targets for FMCW Radar," *IEEE Trans. Aerosp. Electron. Syst.*, vol. 55, no. 4, pp. 2066-2078, Aug. 2019.
- [6] J. Martínez García, D. Zoeke, and M. Vossiek, "MIMO-FMCW Radar-Based Parking Monitoring Application With a Modified Convolutional Neural Network With Spatial Priors," *IEEE Access*, vol. 6, pp. 41391-41398, Jul. 2018.
- [7] H. -S. Lim, H. -M. Park, J. -E. Lee, Y. -H. Kim, and S. Lee, "Lane-by-Lane Traffic Monitoring Using 24.1 GHz FMCW Radar System," *IEEE Access*, vol. 9, pp. 14677-14687, Jan. 2021.
- [8] M. Lee and Y. Kim, "Design and Performance of a 24-GHz Switch-Antenna Array FMCW Radar System for Automotive Applications," *IEEE Trans. Veh. Technol.*, vol. 59, no. 5, pp. 2290-2297, Jun. 2010.
- [9] C. Hu, Y. Liu, H. Meng, and X. Wang, "Randomized Switched Antenna Array FMCW Radar for Automotive Applications," *IEEE Trans. Veh. Technol.*, vol. 63, no. 8, pp. 3624-3641, Oct. 2014.
- [10] H. Jia *et al.*, "A 77 GHz Frequency Doubling Two-Path Phased-Array FMCW Transceiver for Automotive Radar," *IEEE J. Solid-State Circuits*, vol. 51, no. 10, pp. 2299-2311, Oct. 2016.
- [11] K.-T. Kim, I.-S. Choi, and H.-T. Kim, "Efficient radar target classification using adaptive joint time-frequency processing," *IEEE Trans. Antennas Propag.*, vol. 48, no. 12, pp. 1789-1801, Dec. 2000.
- [12] K.-T. Kim, D.-K. Seo, and H.-T. Kim, "Efficient classification of ISAR images," *IEEE Trans. Antennas Propag.*, vol. 53, no. 5, pp. 1611-1621, May 2005.
- [13] M. A. Saville, D. K. Saini, and J. Smith, "Commercial vehicle classification from spectrum parted linked image test-attributed synthetic aperture radar imagery," *IET Radar Sonar Navig.*, vol. 10, no. 3, pp. 569-576, Mar. 2016.
- [14] L. Daniel *et al.*, "Application of Doppler beam sharpening for azimuth refinement in prospective low-THz automotive radars," *IET Radar Sonar Navig.*, vol. 12, no. 10, pp. 1121-1130, Oct. 2018.
- [15] X. Cai and K. Sarabandi, "A Machine Learning Based 77 GHz Radar Target Classification for Autonomous Vehicles," in *Proc. IEEE Int. Symp. Antennas Propag. USNC-URSI Radio Sci. Meeting*, Atlanta, GA,

- USA, 2019, pp. 371-372.
- [16] V. C. Chen, F. Li, S.-S. Ho, and H. Wechsler, "Micro-Doppler Effect in Radar: Phenomenon, Model, and Simulation Study," *IEEE Trans. Aerosp. Electron. Syst.*, vol. 42, no. 1, pp. 2-21, Jan. 2006.
 - [17] L. Du, L. Li, B. Wang, and J. Xiao, "Micro-Doppler Feature Extraction Based on Time-Frequency Spectrogram for Ground Moving Targets Classification with Low-Resolution Radar," *IEEE Sensors J.*, vol. 16, no. 10, pp. 3756-3763, May 2016.
 - [18] O. H. Y. Lam, R. Kulke, M. Hagelen, and G. Möllenbeck, "Classification of Moving Targets Using Micro-Doppler Radar," in *Proc. 17th Int. Radar Symp. (IRS)*, Krakow, Poland, 2016, pp. 1-6.
 - [19] L. Wang and Y. Lu, "Classification and Identification of Micro-Doppler Signatures of Pedestrian and Cyclists Using Simulated Data and ELM," in *Proc. 2019 IEEE International Conference on Signal, Information and Data Processing (ICSIDP)*, Chongqing, China, 2019, pp. 1-4.
 - [20] S. Lee *et al.*, "Classification of Shell-Shaped Targets Using RCS and Fuzzy Classifier," *IEEE Trans. Antennas Propag.*, vol. 64, no. 4, pp. 1434-1443, Apr. 2016.
 - [21] K. Geary, J. S. Colburn, A. Bekaryan, S. Zeng, B. Litkouhi, and M. Murad, "Automotive Radar Target Characterization from 22 to 29 GHz and 76 to 81 GHz," in *Proc. IEEE Radar Conf. (RadarCon13)*, Ottawa, ON, Canada, 2013, pp. 1-6.
 - [22] Y. Lee, H. Choo, S. Kim, and H. Kim, "RCS based target recognition with real FMCW radar implementation," *Microw. Opt. Technol. Lett.*, vol. 58, no. 7, pp. 1745-1750, Jul. 2016.
 - [23] S. Lee, Y.-J. Yoon, J.-E. Lee, and S.-C. Kim, "Human-vehicle classification using feature-based SVM in 77-GHz automotive FMCW radar," *IET Radar Sonar Navig.*, vol. 11, no. 10, pp. 1589-1596, Oct. 2017.
 - [24] B. H. Borden, "Enhanced range profiles for radar-based target classification using monopulse tracking statistics," *IEEE Trans. Antennas Propag.*, vol. 43, no. 8, pp. 759-765, Aug. 1995.
 - [25] K.-T. Kim, D.-K. Seo, and H.-T. Kim, "Efficient radar target recognition using the MUSIC algorithm and invariant features," *IEEE Trans. Antennas Propag.*, vol. 50, no. 3, pp. 325-337, Mar. 2002.
 - [26] I. Urazghildiev *et al.*, "Vehicle Classification Based on the Radar Measurement of Height Profiles," *IEEE Trans. Intell. Transp. Syst.*, vol. 8, no. 2, pp. 245-253, Jun. 2007.
 - [27] J. A. Garzon-Guerrero, D. P. Ruiz, and M. C. Carrion, "Classification of Geometrical Targets Using Natural Resonances and Principal Components Analysis," *IEEE Trans. Antennas Propag.*, vol. 61, no. 9, pp. 4881-4884, Sept. 2013.
 - [28] Y. Kim, I. Alnujaim, S. You, and B. J. Jeong, "Human Detection Based on Time-Varying Signature on Range-Doppler Diagram Using Deep Neural Networks," *IEEE Geosci. Remote Sens. Lett.*, vol. 18, no. 3, pp. 426-430, Mar. 2021.
 - [29] A. Angelov, A. Robertson, R. Murray-Smith, and F. Fioranelli, "Practical classification of different moving targets using automotive radar and deep neural networks," *IET Radar Sonar Navig.*, vol. 12, no. 10, pp. 1082-1089, Oct. 2018.
 - [30] B. Dekker, S. Jacobs, A. S. Kossen, M. C. Kruithof, A. G. Huizing, and M. Geurts, "Gesture recognition with a low power FMCW radar and a deep convolutional neural network," in *Proc. Eur. Radar Conf. (EURAD)*, Nuremberg, Germany, 2017, pp. 163-166.
 - [31] Z. Zhang, Z. Tian, and M. Zhou, "Latent: Dynamic Continuous Hand Gesture Recognition Using FMCW Radar Sensor," *IEEE Sensors J.*, vol. 18, no. 8, pp. 3278-3289, Apr. 2018.
 - [32] H. -S. Lim, J. Jung, J. -E. Lee, H. -M. Park, and S. Lee, "DNN-Based Human Face Classification Using 61 GHz FMCW Radar Sensor," *IEEE Sensors J.*, vol. 20, no. 20, pp. 12217-12224, Oct. 2020.
 - [33] B. Vandersmissen *et al.*, "Indoor Person Identification Using a Low-Power FMCW Radar," *IEEE Trans. Geosci. Remote Sens.*, vol. 56, no. 7, pp. 3941-3952, Jul. 2018.
 - [34] S. A. Shah and F. Fioranelli, "Human Activity Recognition: Preliminary Results for Dataset Portability using FMCW Radar," in *Proc. Int. Radar Conf. (RADAR)*, Toulon, France, 2019, pp. 1-4.
 - [35] F. Qi *et al.*, "Position-Information-Indexed Classifier for Improved Through-Wall Detection and Classification of Human Activities Using UWB Bio-Radar," *IEEE Antennas Wireless Propag. Lett.*, vol. 18, no. 3, pp. 437-441, Mar. 2019.
 - [36] M. I. AlHajri, N. T. Ali, and R. M. Shubair, "Classification of Indoor Environments for IoT Applications: A Machine Learning Approach," *IEEE Antennas Wireless Propag. Lett.*, vol. 17, no. 12, pp. 2164-2168, Dec. 2018.
 - [37] S. Kim, S. Lee, S. Doo, and B. Shim, "Moving Target Classification in Automotive Radar Systems Using Convolutional Recurrent Neural Networks," in *Proc. 26th Eur. Signal Process. Conf. (EUSIPCO)*, Rome, Italy, 2018, pp. 1482-1486.
 - [38] K. Patel, K. Rambach, T. Visentin, D. Rusev, M. Pfeiffer, and B. Yang, "Deep Learning-Based Object Classification on Automotive Radar Spectra," in *Proc. IEEE Radar Conf. (RadarConf)*, Boston, MA, USA, 2019, pp. 1-6.
 - [39] R. Pérez, F. Schubert, R. Raschofer, and E. Biebl, "Single-Frame Vulnerable Road Users Classification with a 77 GHz FMCW Radar Sensor and a Convolutional Neural Network," in *Proc. 19th Int. Radar Symp. (IRS)*, Bonn, Germany, 2018, pp. 1-10.
 - [40] A. Palfy, J. Dong, J. F. Kooij, and D. M. Gavrila, "CNN based Road User Detection using the 3D Radar Cube," *IEEE Robotics Automation Letters*, vol. 5, no. 2, pp. 1263-1270, Apr. 2020.
 - [41] X. Chen, *Computational Methods for Electromagnetic Inverse Scattering*. Wiley-IEEE, 2018, pp. 129-138.
 - [42] K. Tan and X. Chen, "Fast 3-D Image Reconstruction on Nonregular UWB Sparse MIMO Planar Array Using Scaling Techniques," *IEEE Trans. Microw. Theory Techn.*, vol. 69, no. 1, pp. 222-234, Jan. 2021.
 - [43] D. P. Kingma and J. Ba. (2015, May). Adam: A method for stochastic optimization. Presented at Int. Conf. Learn. Represent. [Online]. Available: <https://arxiv.org/pdf/1412.6980.pdf>
 - [44] G. Gao, L. Liu, L. Zhao, G. Shi, and G. Kuang, "An Adaptive and Fast CFAR Algorithm Based on Automatic Censoring for Target Detection in High-Resolution SAR Images," *IEEE Trans. Geosci. Remote Sens.*, vol. 47, no. 6, pp. 1685-1697, Jun. 2009.
 - [45] Y. Cheng, F. X. Yu, R. S. Feris, S. Kumar, A. Choudhary, and S. Chang, "An Exploration of Parameter Redundancy in Deep Networks with Circulant Projections," in *Proc. IEEE Int. Conf. Comput. Vis. (ICCV)*, Santiago, Chile, 2015, pp. 2857-2865.
 - [46] M. Grandini, E. Bagli, and G. Visani. (2020, Aug.). Metrics for Multi-Class Classification: an Overview. E-print arXiv:2008.05756 [Online]. Available: <https://arxiv.org/pdf/2008.05756.pdf>



Kai Tan received the Ph.D. degree in electrical engineering from University of Chinese Academy of Sciences, Beijing, China, in 2016. From 2016 to 2019, he was a Research Assistant with the Institute of Acoustics, Chinese Academy of Sciences, Beijing, China. From 2019 to 2021, he was a Research Fellow with the National

University of Singapore, Singapore. Since 2021, he has been an Associate Professor with the Key Laboratory of Electromagnetic Waves (Ministry of Education), School of Information Science and Technology, Fudan University, Shanghai, China. His research interests include mainly radar system design and data processing. He is currently working on intelligent radar sensing techniques for various applications, such as autonomous driving, intelligent surveillance, unmanned aerial vehicle airborne synthetic aperture radar, etc. Dr. Tan has published more than 20 papers on microwave theory and radar techniques. He also serves as a Reviewer for many journals including *IEEE Transactions on Antennas and Propagation* and *IEEE Antennas and Wireless Propagation Letters*.



Tiantian Yin received the B.E. degree (with First-Class Hons.) in electrical and electronic engineering from Nanyang Technological University, Singapore, in 2016 and the Ph.D. degree in electrical and computer engineering from the National University of Singapore, Singapore, in 2021. She is currently a Research Fellow

with the National University of Singapore, Singapore. Her research interests include electromagnetic inverse scattering problems. Dr. Yin was a recipient of the 2020 Best Student Paper Competition Award from the IEEE Singapore Microwave Theory and Techniques/Antennas and Propagation (MTT/AP) Chapter.



Ruan Hongning received the Bachelor and Master degrees in automation from Northwestern Polytechnical University, China, in 1994 and 1997, respectively. She received the Master of engineering degree in electrical engineering from Nanyang Technological University (NTU), Singapore, 2000. From 2000 to 2018, she

was with sensor division of DSO National Laboratories. As a senior member of technical staff, she worked on remote sensing image exploitation. She joined Desay SV Singapore in 2018, where she is currently a Senior Principal Engineer. Her research interests include radar signal processing, Direction-of-Arrival, synthetic aperture radar imaging and image analysis.



Siegfried Balon (M'14) received the B.S. and M.S. degrees from the University of the Philippines – Diliman in 2009 and 2011, respectively, and the Ph.D. degree from the National University of Singapore (NUS) in 2019. He was a research fellow at NUS before joining Desay SV Singapore in 2019 where he

is currently a Principal Engineer. His research interests include microwave and RF systems, synthetic aperture radar imaging, digital beamforming and MIMO radars, algorithm design for automotive radars and sensor fusion technologies.



Xudong Chen (Fellow, IEEE) received the B.S. and M.S. degrees from Zhejiang University, China, in 1999 and 2001, respectively, and the Ph.D. degree from the Massachusetts Institute of Technology, Cambridge, MA, USA, in 2005. Since 2005, he has been with the National University of Singapore, Singapore, where he is currently a Professor. He has

published 160 journal papers on inverse scattering problems, material parameter retrieval, microscopy, and optical encryption. He has authored the book *Computational Methods for Electromagnetic Inverse Scattering* (Wiley-IEEE, 2018). His research interests include mainly electromagnetic wave theories and applications, with a focus on inverse problems and computational imaging. He is recently working on mm-wave imaging algorithms and solving inverse problems via machine learning. Dr. Chen was a recipient of the Young Scientist Award by the Union Radio Scientifique Internationale in 2010 and a recipient of the Ulrich L. Rohde Innovative Conference Paper Award at ICCEM 2019 conference. He was an Associate Editor of the *IEEE Transactions on Microwave Theory and Techniques* during 2015-2019 and is currently an Associate Editor of *IEEE Transactions on Geoscience and Remote Sensing* and *IEEE Journal of Electromagnetics, RF and Microwave in Medicine and Biology*. He has been members of organizing committees of more than 10 conferences, serving as General Chair, TPC Chair, Award Committee Chair, etc. He was the Chair of IEEE Singapore MTT/AP Joint Chapter in 2018. He is a Fellow of Electromagnetics Academy.